Lattice dynamics and elasticity of $SrCO_3$

Tra Nguyen-Thanh,[a,b]* Alexei Bosak,[b] Johannes D. Bauer,[a] Rita Luchitskaia,[a] Keith Refson,[c,d] Victor Milman[e] and Bjoern Winkler[a]

[a]*Institute of Geosciences, University of Frankfurt, Altenhoeferallee 1, Frankfurt a.M., 60438, Germany,* [b]*ESRF - The European Synchrotron, 71 Avenue des Martyrs, Grenoble, F-38000, France,* [c]*ISIS Facility, RAL, Chilton, Didcot OX11 0QX, United Kingdom,* [d]*Department of Physics, Royal Holloway University of London, Egham, Surrey TW20 0EX, United Kingdom, and* [e]*BIOVIA Dassault Systmes, 334 Science Park, Cambride, CB4 0WN, United Kingdom. E-mail: thanh-tra.nguyen@esrf.fr*

Lattice dynamics; SrCO3; Phonon; IXS; inelastic X-ray scattering; TDS; thermal diffuse scattering; DFT; elasticity

Abstract

The lattice dynamics and elasticity of synthetic $SrCO_3$ have been investigated by a combination of *ab initio* lattice dynamics calculations, microcalorimetry, Raman spectroscopy, X-ray thermal diffuse scattering and high resolution inelastic X-ray scattering. The results of density functional based calculations were in all cases in good agreement with experiment. For the spectroscopic investigations, peak positions and intensities are well reproduced by the DFT model. Experimentally determined intensity distributions in thermal diffuse scattering maps differ from the theoretical

distribution only in the HK0 plane, which we assign to stacking disorder. As the model is accurate and reliable, we predict the complete elastic stiffness tensor and, on the basis of these results, discuss the anisotropy of the sound velocities, also in relation to the anisotropy in other carbonate systems.

1. Introduction

Carbonates are considered the most stable carbon-bearing source in the Earth lower-mantle (Luth, 1999). They are geologically interesting because understanding their dynamics and physical properties could help researchers to estimate the carbon budget of the Earth (Dasgupta & Hirschmann, 2010; Hazen *et al.*, 2013). In this context, most of important carbonates such as calcite, $CaCO_3$, dolomite $CaMg[CO_3]_2$ and magnesite, $MgCO_3$, and their respective polymorphs are extensively studied (Reeder, 1983; Luth, 1999). Consequently, the $CaCO_3$ polymorphs calcite and aragonite are by far the most studied carbonates with respect to their lattice dynamics and phase transitions at high pressure and temperature (Dove *et al.*, 1992; Singh *et al.*, 1987; Plihal & Schaack, 1970; Plihal, 1973; Ye *et al.*, 2012; Lin & Liu, 1997*a*; Arapan & Ahuja, 2010; Fiquet *et al.*, 1994). These studies are facilitated by the ubiquity of large calcite crystals of excellent quality.

However, in order to gain a deeper understanding of the structure-property relations in carbonates, it is also necessary to understand the behavior of other carbonates. While there have been comparative crystal chemical studies with respect to structural parameters and properties such as the compressibility (Zhang & Reeder, 1999), the lattice dynamics of other carbonates have not been studied in depth. A typical case is strontianite, $SrCO_3$, which is a representative of carbonates with large cations, which crystallize in the aragonite structure type, with orthorhombic symmetry (space group *Pmcn*) with Z = 4 formula units per unit cell (Fig. 1). The CO_3 groups are aligned

parallel to the (001) planes. Earlier studies of the lattice dynamics of $SrCO_3$ have been limited to the determination of Γ-point phonons using Raman (Krishnan, 1956; Krishnamurti, 1960; Gillet *et al.*, 1993; Lin & Liu, 1997*b*; Buzgar & Apopei, 2009) or infrared absorption spectroscopy (Huang & Kerr, 1960; Adler & Kerr, 1963; Chester & Elderfield, 1967).

As with other carbonates, pressure-induced phase transitions of $SrCO_3$ were subject of numerous studies (Ye *et al.*, 2012; Lin & Liu, 1997*a*; Arapan & Ahuja, 2010; Lin & Liu, 1997*b*; Ono *et al.*, 2005; Sanchez-Valle *et al.*, 2003; Wang *et al.*, 2015). However, there is still an on-going controversy concerning the pressure-induced phase transitions of $SrCO_3$. As an example, Lin & Liu (1997*b*) reported a new phase of $SrCO_3$ with the space group $P2_122$ at 35 GPa using Raman spectroscopy, whereas Ono *et al.* (2005) claimed that the phase transition takes place at 10 GPa and the new space group was $P2_12_12$. First principles electronic structure calculations of Arapan & Ahuja (2010) predicted that strontianite would transform from the aragonite-structure type into a new phase with the space group *Pmmn* at 17 GPa. In order to benchmark theoretical models and hence assess their predictive power, it is worthwhile to compare structure-property relations beyond structural parameters such as lattice parameters and interatomic distances. One rather sensitive test is the evaluation of the elastic stiffness tensor, which represents the interatomic interactions. However, details of the elastic behavior of $SrCO_3$ are also unknown, except for the bulk modulus, which was measured by Martens *et al.* (1982) who obtained a value for $B = 58 \pm 10$ GPa and, more recently, by Wang *et al.* (2015) who gave $B = 62 \pm 1$ GPa.

The present study aims to provide a full description of the lattice dynamics and elasticity of $SrCO_3$ through a combination of *ab initio* calculations and experimental measurements using microcalorimetry, Raman spectroscopy, X-ray thermal diffuse scattering (TDS) and inelastic X-ray scattering (IXS), and compare these findings to

studies of other carbonates. Furthermore, the validity of our theoretical calculations as confirmed by experimental measurements would provide stringent benchmarks for future studies on the lattice dynamics and stabilities at extreme (high pressure, temperature) conditions.

2. Experimental

2.1. Samples preparation

First, strontium nitrate $Sr(NO_3)_2$ (0.01 mol) was dissolved in 50 ml bidistilled water. The salt solution was added dropwise to 100 ml of a precipitant solution of ammonium bicarbonate, NH_4HCO_3, (0.002 mol) while stirring at ambient temperature. The resulting suspension was transferred into a 60 ml Teflon cup, filling it up to 60% of its capacity. Subsequently, the cup was put into a stainless steel autoclave and sealed tightly. After reaction at 493 K for 24 hours, the autoclave was slowly cooled down (493 K - 453 K in 48 hours, then 453 K to ambient temperature in 24 hours). The precipitate obtained was filtered under vacuum, washed repeatedly with distilled water and dried at 333 K. Powder X-ray diffraction (Cu-$K_{\alpha 1}$ from curved Ge (110) monochromator, 40 kV, 30 mA, X'pert PRO diffractometer from PANalytical) showed no phases other than strontianite. Visual inspection of the product showed two distinct growth morphologies. While most of the sample was a fine powder, some optically transparent individual crystals with up to 100 m edge length were present. Later inspection showed that these were twinned specimen.

2.2. Raman spectroscopy

Raman spectra were obtained from the synthetic samples using a micro-Raman spectrometer (Renishaw). We employed the 532 nm line of a Nd:YAG laser, using 10% - 33% of the maximum power of 200 mW and obtained spectra in 20 - 30 s in

the frequency range from 100 - 2000 cm^{-1}.

2.3. TDS and IXS measurement

The X-ray thermal diffuse scattering (TDS) measurement was performed in transmission geometry on the beamline ID29 (de Sanctis *et al.*, 2012) at the ESRF using a monochromatic beam of 15.50 keV, which is below the absorption edge of strontium. The samples were rotated with an increment of 0.1° orthogonal to the beam direction over an angular range of 360°, while the diffuse scattering patterns were recorded using a Pilatus 6M detector (Kraft *et al.*, 2009). The orientation matrix and geometry of the experiment were refined using the CrysAlis software package, which allowed the reconstruction of 2D reciprocal space maps. These TDS maps were then compared with calculated maps using a program written by Wehinger *et al.* (2014).

The single crystal IXS measurements were carried out on the ID28 beamline at the ESRF. The spectrometer was operated at 17.794 keV incident energy which corresponds to a wavelength of 0.6968 Å, providing an energy resolution of 3.0 meV full width at half maximum with a focused beam size of 50 m × 50 m. Energy transfer scans at constant momentum transfer (Q) were performed in transmission geometry along selected directions in reciprocal space. All of the measurements were carried out at ambient pressure and temperature. Further details of the experimental setup and the data treatment can be found elsewhere (Krisch & Sette, 2006).

2.4. Heat capacity measurement

Heat capacity in the temperature range between 2 K and 395 K were measured employing a Quantum Design Physical Properties Measurement System (PPMS). A powder sample of 14.98 mg $SrCO_3$ was compressed into a small Cu-crucible, weighing 12.08 mg. The heat capacity of the Cu-crucible was determined separately and

subtracted from the total heat capacity. The accuracy of the mass determination was about ± 0.02 mg. Data were collected at 150 temperatures, where the temperature difference between subsequent steps was increased logarithmically from low to high temperatures. At each temperature three responses to a heat pulse were measured and analyzed with the MultiVu software.

The accuracy of our heat capacity measurements was determined by measurements of Al_2O_3 (SRM-720) and Cu (99.999 %, Alfa Aesar) reference materials. A comparison of our data for SRM-720 with that published by Ditmars *et al.* (1982) gives a deviation of 2 % in the range between 395 K and 50 K and 6 % below 5 K. The heat capacity data of the Cu sample is compared to that of Lashley *et al.* (2003), the deviation is less than 1 % in the temperature range between 300 K and 40 K and 2 % below 40 K.

3. Lattice dynamics calculations

DFT calculations were performed with commercial and academic versions of the CASTEP program (Clark *et al.*, 2009) using the generalized gradient approximation (GGA) formalized by Perdew-Burke-Ernzerhof (PBE) (Perdew *et al.*, 1996) or the WC approximation with a plane wave basis set and q_c-optimized norm-conserving pseudopotentials (Rappe *et al.*, 1990). The maximum cutoff energy of the plane waves was 900 eV. An 8 × 4 × 6 Monkhorst-Pack grid (Monkhorst & Pack, 1976) was employed for sampling of reciprocal space corresponding to a k-point separation of less than 0.030 $Å^{-1}$. Spectroscopic and thermal properties including phonon frequencies, IR and Raman intensities and the low-temperature heat capacity were obtained within the formalism of harmonic ab initio lattice dynamics using density-functional perturbation theory (DFPT) (Refson *et al.*, 2006). Computed IR and Raman spectra were artificially broadened in order to mimic an instrumental resolution function of 5

cm^{-1}.

Scattering intensities for inelastic and thermal diffuse scattering were calculated in the first order approximation (Xu & Chiang, 2009; Krisch & Sette, 2006). The frequencies and mode polarization information required were taken from the DFPT lattice dynamics calculations. The momentum transfer dependence of the atomic scattering factor was taken into account using an analytic function with coefficients derived from Hartree-Fock wave functions (Cromer & Mann, 1968). IXS spectra are resolved in phonon energy and the intensity is sensitive to the eigenvectors. TDS intensities are not resolved in energies, but due to their strong energy dependence, i.e. $I(\boldsymbol{Q}) \propto \frac{1}{\omega(\boldsymbol{q})} coth(\frac{\hbar\omega(\boldsymbol{q})}{2k_BT}) f(\boldsymbol{Q})^2$ where $\boldsymbol{Q}$ the momentum transfer, $\boldsymbol{q}$ the reduced momentum transfer, $\omega = E/\hbar$ the phonon frequency, $f(\boldsymbol{Q})$ the atomic scattering factor, they are sensitive to low energy excitations.

4. Results and discussion

The structure of strontianite is well-reproduced by the DFT-based calculations. Depending on the exchange-correlation potential employed, the fully relaxed structural parameters deviate by only 1% from the experimental values. This is in agreement with the results of similar studies on other carbonates (Skinner *et al.*, 1994; Winkler *et al.*, 2000; Medeiros *et al.*, 2006; Medeiros *et al.*, 2007; Hossain *et al.*, 2010; Hossain *et al.*, 2011; Brik, 2011).

The computed Raman and IR spectra are compared to experimental data in Fig. 2.

As is obvious from these figures, both positions and intensities of the peaks are very well reproduced. The error in the computed frequencies is a few percent only. This good agreement allows an unambiguous assignment of Raman and IR bands to specific polarization vectors.

The eigenfrequencies and eigenvectors produced from the DFPT-based calculations

are employed to calculate TDS intensity distributions. Figure 3 shows high symmetry reciprocal space sections of calculated and experimental TDS intensity maps. The experimental maps show signatures of stacking faults which appear as streaky features around the Bragg reflections in the HK0 plane. Diffuse scattering signal from acoustic phonons are observable close to Bragg reflections in the ⟨110⟩ and ⟨011⟩ directions in the HK0 and 0KL planes, and along ⟨001⟩ directions in the HHL plane. A very good agreement between the simulated and measured TDS maps is observed from this figure.

Phonon dispersion curves are measured along ⟨001⟩ and ⟨110⟩ directions in the energy range from -20 meV to 40 meV. Eight spectra are measured along the ⟨001⟩ direction whereas the ⟨110⟩ direction consists of five measured spectra. Fig. 4 a-b) show the individual experimental IXS spectra in comparison with calculated IXS spectra. The corresponding q vectors are indicated on the graphs. The intensities of both calculated and measured spectra are normalized for comparison. The spectra at different q vectors are shifted for ease of visualization. One can see a very good matching between the calculated and measured spectra at different q vectors. This agreement is presented on Fig. 4 c) where measured phonon energies are compared with theoretical values. The solid red line represents the ideal agreement between calculated and measured phonon frequencies (i.e. $E_{exp.} = E_{calc.}$) at different q vectors. These results imply that our model calculations correctly predict both the eigenvectors and eigenfrequencies of $SrCO_3$ at any arbitrary momentum transfer.

The experimental IXS spectra are employed to plot the IXS intensity maps. Fig. 5 shows the experimental maps alongside the corresponding calculated maps. The measured IXS intensity maps are shown on the left panel for ⟨001⟩ (first row) and ⟨110⟩ (second row) directions the directions are indicated on the maps; the corresponding computed dispersion curves are shown on the right panel for comparison. Both maps

are measured with linear Q-spacing and energy step of 0.68 meV. The momentum- and energy-transfers are linearly interpolated to 40 q-points and 100 energy steps. Note that the elastic lines are subtracted from these experimental maps. For the theoretical maps, the inelastic intensity is calculated from the eigenvectors and eigenfrequencies for 200 q-points along the given direction in reciprocal space and convoluted with the experimental resolution function of the spectrometer. The measured phonons (black points) are presented on the computed IXS intensity maps showing a very good agreement between calculation and experiment, as we have seen on Fig 4 c).

The computed phonon density of states (PDOS) of $SrCO_3$ is shown on Fig. 6, where the contributions of the individual atomic species are also given. This partial density of states shows, as expected, that the low frequency phonons are dominated by the vibration of the strontium atoms, while at high frequencies the polarization vectors are dominated by displacements of carbon and oxygen.

The phonon density of states has then been used to compute the temperature dependence of the heat capacity in the harmonic approximation. Figure 7 shows our experimental measurement of the heat capacity of synthetic $SrCO_3$ in comparison with DFT-based calculations and experimental data extracted from the work of Gurevich *et al.* (2001). The heat capacity of $SrCO_3$ is well reproduced by our calculations. We expect the theoretical value to be slightly lower at high temperatures due to the neglect of anharmonicity. Above 200 K, the heat capacities measured by Gurevich *et al.* (2001) are higher than our values. Gurevich *et al.* (2001) used much larger natural samples and hence we attribute the discrepancy between our and their data to impurities in their natural samples.

The accuracy of our calculations allows us to predict the elastic stiffness coefficients of $SrCO_3$. Because of the orthorhombic symmetry, the elastic tensor of $SrCO_3$ contains 9 independent elements (C_{11}, C_{22}, C_{33}, C_{44}, C_{55}, C_{66}, C_{12}, C_{13} and C_{23}). These 9

coefficients are reported in Table 1. The bulk modulus is also computed using the Voigt Reuss Hill average scheme (Hill, 1952). This value is $B = 62.95 \pm 3$ GPa which is in good agreement with experimental measurements from the literature ($B = 62 \pm 1$ GPa (Wang *et al.*, 2015) and $B = 58 \pm 10$ GPa (Martens *et al.*, 1982). From the measured phonon dispersion curves along the $\langle 001 \rangle$ direction we have obtained C_{33} using the longitudinal acoustic phonon at q = (0 0 3.8), which is close to the Γ-point (0 0 4). Because of the intense elastic line near the Γ-point, acoustic phonons closer to (0 0 4) could not be measured. This acoustic phonon energy gives $C_{33} = 75.4 \pm 1.4$ GPa which is very close to our theoretical value $C_{33} = 74 \pm 1$ GPa, thus providing another indication for the reliability of our computational approach.

The acoustic velocity profiles along the three principle directions (X, Y, Z) which are respectively parallel to the *a, b* and *c* axis of the unit cell, are calculated using the Christoffel equations (Ledbetter & Kriz, 1982). The representation surface of the longitudinal effect of $SrCO_3$ elastic tensor is also calculated using the following equation (Arbeck *et al.*, 2012):

$$F = \sum_{i,j,k,l} x_i x_j x_k x_l C_{ijkl} \tag{1}$$

where $\begin{pmatrix} x_1 \\ x_2 \\ x_3 \end{pmatrix}$ are the Cartesian components of the direction vectors $\boldsymbol{x}$ which describe a unit sphere, i, j, k, l take the values {1, 2, 3} and C_{ijkl} are the elastic coefficients.

The velocity profiles and the tensor surface are presented in Fig. 8. In an anisotropic material, wave energy may propagate in two modes: longitudinal and shear (or transverse). In general the faster mode is the longitudinal mode where the vibration of particles is parallel to the propagation of wave energy. The shear mode is the slower mode where the particle vibrations are normal to the propagation direction, thus this mode has two sub-modes corresponding to the two directions perpendicular to the propagation direction. The direction of the particle vibration is referred to as the

polarization. As we can observe in Fig. 8 a-c), the longitudinal waves (V_P) always travel with the highest speed, whereas the shear waves V_{S1} and V_{S2} are sometimes crossed each other. The images immediately show strong anisotropy of the sound velocities in strontianite.

The elastic anisotropy of $SrCO_3$ can be further quantified by evaluating the acoustic velocities for each direction of interest (X_i) over a hemisphere. The three velocities are obtained by solving for the eigenvalues of the symmetric Christoffel stiffness matrix (Mainprice, 1990). The azimuthal V_P and V_S (V_{S1} and V_{S2}: the two quasi-transverse waves) anisotropies can be analysed using the anisotropy factors introduced by Mainprice *et al.* (2000). The anisotropy factor for V_P (A_P) and V_S (A_S) are defined as:

$$\begin{aligned} A_P &= 2 \times \frac{V_{P,max} - V_{P,min}}{V_{P,max} + V_{P,min}} \times 100\% \\ A_S &= 2 \times \frac{V_{S1} - V_{S2}}{V_{S1} + V_{S2}} \times 100\% \end{aligned} \tag{2}$$

where $V_{P,max}$ and $V_{P,min}$ represent the maximum and minimum V_P velocities in all directions. Fig. 9 a) presents the distribution of V_P in a hemisphere pointing toward the Z direction ($\langle 001 \rangle$). This result gives an anisotropy factor $A_P = 35.61$ % for the V_P wave. The distribution of A_S (also called the shear-wave splitting factor) is represented in Fig. 9 b) which gives a maximum anisotropy factor A_S of 22.34 %.

In order to assess the reliability of our calculations, we carried out an analogous analysis for aragonite. The computed and experimentally determined C_{ij}, where the latter were taken from Liu *et al.* (2005), are given in Table 2.

The agreement between the experimentally determined and computed C_{ij} are typical for the accuracy of DFT-based models, where a discussion on the role of the choice for the exchange-correlation potential has been given by Winkler & Milman (2014). Fig. 10 shows how the anisotropy of the velocities depends on the differences in the C_{ij} anisotropy of other carbonate systems. Clearly, the anisotropy in V_P is very well

reproduced, both in terms of direction and magnitude. For V_S, the directionality is well reproduced, but the magnitude of the anisotropy differs by ~ 22 %.

While further studies on other orthorhombic carbonates need to be carried out, it is to be expected that the distribution of the anisotropy will be similar for isostructural compounds. We then compare the anisotropy factors of orthorhombic carbonates to that of calcite, siderite and magnesite, the rhombohedral carbonates, in Fig. 10. The experimental values are from (Chen *et al.*, 2001; Liu *et al.*, 2005; Sanchez-Valle *et al.*, 2011) and all anisotropy factors are summarized in Table 3. We find that the magnitude of the anisotropy factors is similar, independent of the crystal structure of the carbonates.

5. Conclusions

A complete description of the lattice dynamics and elasticity of strontianite, $SrCO_3$, is reported for the first time through a combination of *ab initio* calculations and experimental measurement using microcalorimetry, Raman spectroscopy, TDS and high resolution IXS. Our experimental observations are very well reproduced by our calculations, thus allowing us to confidently predict the full elastic stiffness tensor of $SrCO_3$. The calculated bulk modulus in this work is in good agreement with the measurements reported in the literature. Strong elastic anisotropy is observed by evaluating the acoustic velocities of $SrCO_3$ in all directions. A comparison of several carbonate systems shows that the elastic anisotropy factors are similar and independent of the crystal structure of the carbonates. The validation of our theoretical model by means of experimental data provides a stringent benchmark for future studies on the lattice dynamics and stabilities of $SrCO_3$ at relevant conditions (high pressure, high temperature) of the Earth lower-mantle.

The authors would like to acknowledge the funding from the German BMBF (project

05K13RF2), the German Science Foundation DFG (project Wi1232 and FOR2125 "CarboPaT") and the French National Research Agency (ANR). The Raman spectra were measured by Javier Ruiz-Fuertes and Michal Stekiel.

Table 1. *Computed elastic stiffness coefficients and bulk modulus of $SrCO_3$ (GPa)*

Elastic coefficients			Bulk modulus B	
	Calculation	Experiment		
C_{11}	150(1)		This work	62.95 ± 3.0
C_{22}	109(1)		Wang *et al.* (2015)	62 ± 1
C_{33}	74(1)	75.4 ± 1.4	Martens *et al.* (1982)	58 ± 10
C_{44}	34(1)			
C_{55}	26(1)			
C_{66}	38(1)			
C_{12}	54(1)			
C_{13}	33(1)			
C_{23}	43(1)			

Table 2. *Calculated and experimental elastic coefficients of aragonite (GPa)*

	Our calculation	Exp. values from Liu *et al.* (2005)
C_{11}	172 (4)	171.1 ± 1.0
C_{22}	113 (7)	110.1 ± 0.9
C_{33}	100.2 (4)	98.4 ± 1.2
C_{44}	37.2 (1)	39.3 ± 0.6
C_{55}	21 (1)	24.2 ± 0.4
C_{66}	41 (3)	40.2 ± 0.6
C_{12}	55 (6)	60.3 ± 1.0
C_{13}	33.4 (8)	27.8 ± 1.6
C_{23}	46.4 (9)	41.9 ± 2.0

Table 3. *Anisotropy factors for other carbonate systems*

	Calc. Aragonite (our work)	Exp. Aragonite Liu *et al.* (2005)	Calcite Chen *et al.* (2001)	Siderite Sanchez-Valle *et al.* (2011)	Magnesite Sanchez-Valle *et al.* (2011)
A_P (%)	29.39	29.62	32.38	31.1	27.0
A_S max. (%)	33.14	25.86	58.92	34.17	35.91

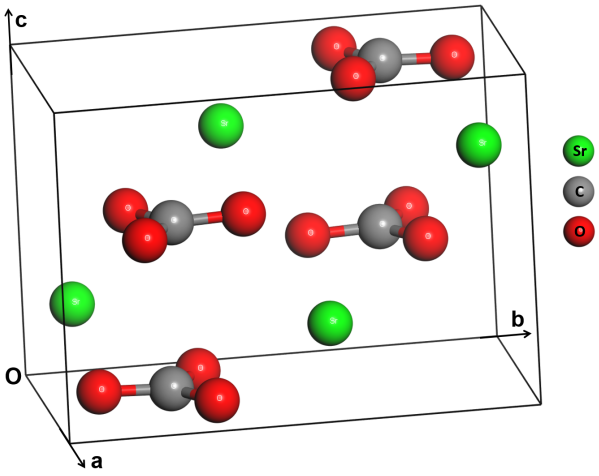

Fig. 1. *Pmcn* orthorhombic structure of strontianite $SrCO_3$

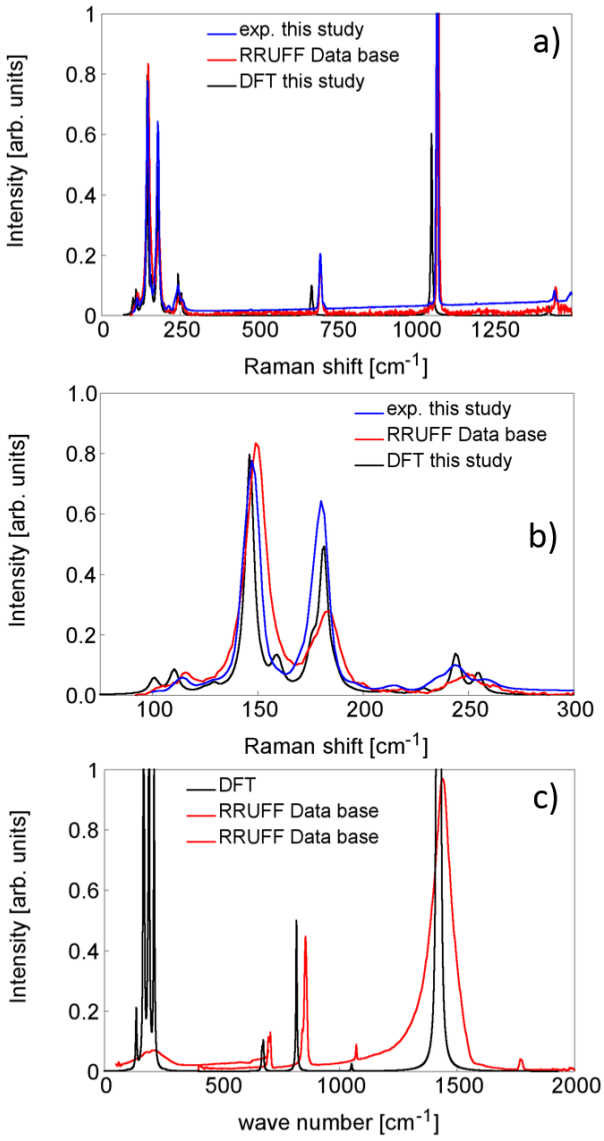

Fig. 2. Measured and calculated Raman (a-b) and IR (c) spectra of synthetic $SrCO_3$. Spectra of natural samples taken from the RRUFF database (Lafuente *et al.*, 2015) are also presented

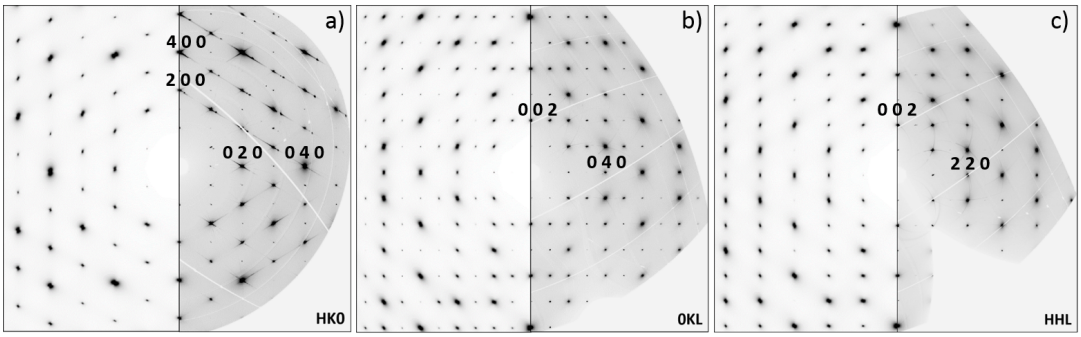

Fig. 3. Calculated diffuse scattering (left part of the individual panels) and experimental (right part of the individual panels) TDS intensity distribution of $SrCO_3$ in the indicated reciprocal space sections.

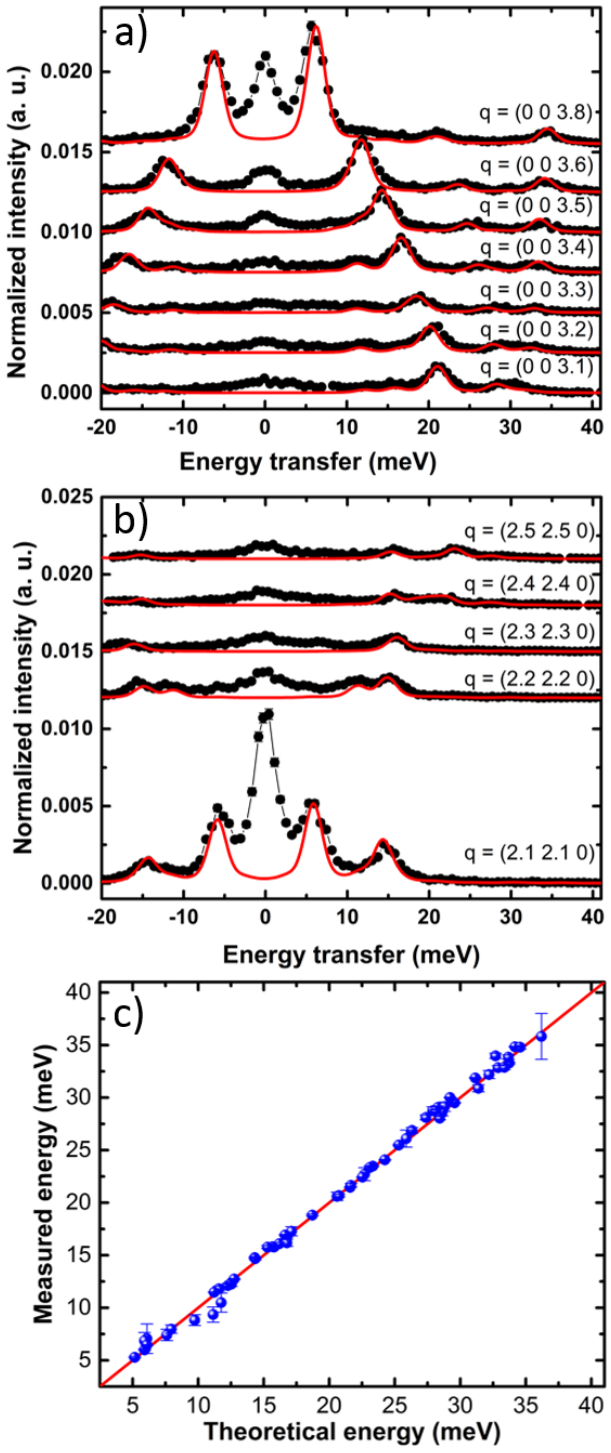

Fig. 4. (a-b) IXS spectra at different wave vectors. Black connected points are measured IXS data; red solid curves are calculated IXS spectra. c) Agreement between the theoretical and measured phonon energies at different wave vectors.

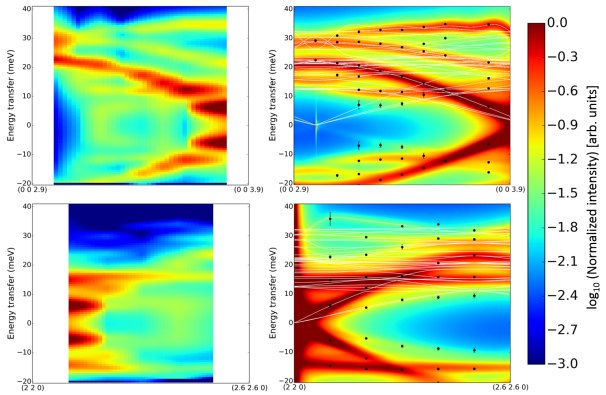

Fig. 5. Measured (left panel) and calculated (right panel) IXS maps. The measured points are presented on the corresponding calculated maps as well. The elastic lines are subtracted from the measured maps. The intensity is in log scale. The intensity scale is adjusted for ease of visualization. The calculated phonon dispersion curves are presented in white solid curves.

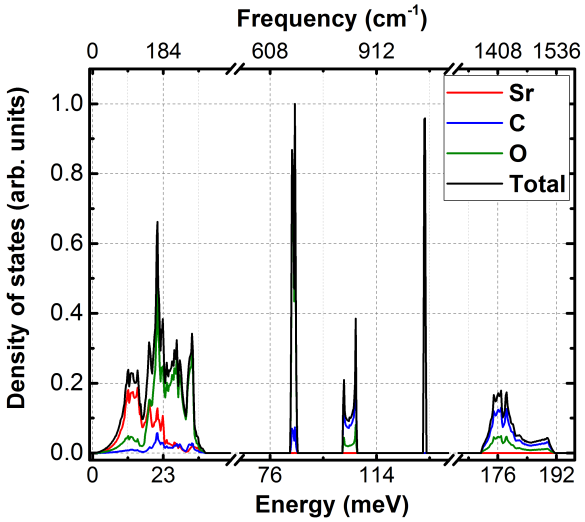

Fig. 6. Calculated phonon density of states of $SrCO_3$

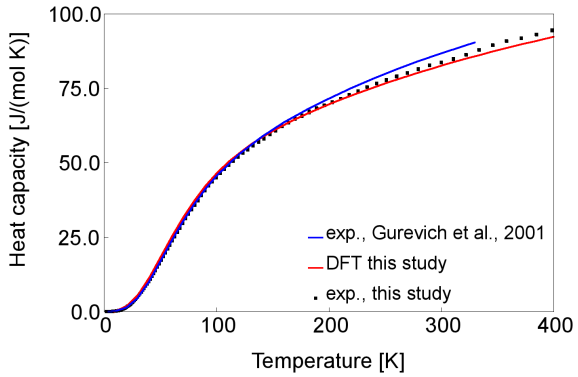

Fig. 7. Heat capacity of $SrCO_3$ measured at different temperature in comparison with DFT-based calculations and experimental measurement of Gurevich *et al.* (2001).

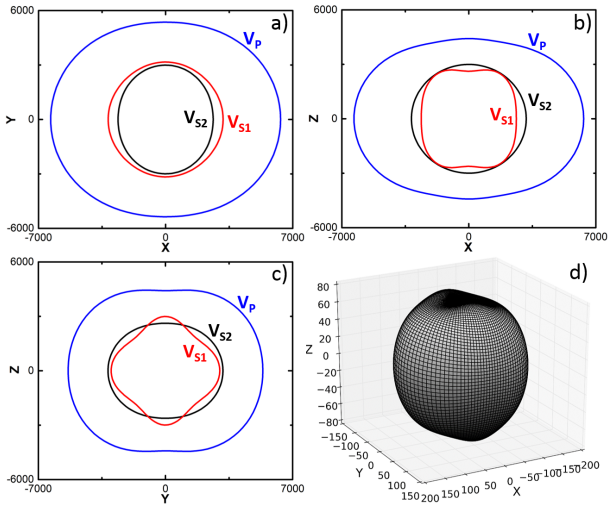

Fig. 8. a)-c): Velocity profiles (m/s) of $SrCO_3$ in the three main orthogonal planes. X, Y and Z are parallel to a, b and c axis of the unit cell, respectively. d): Representation surface of the longitudinal part of the elastic stiffness tensor of $SrCO_3$.

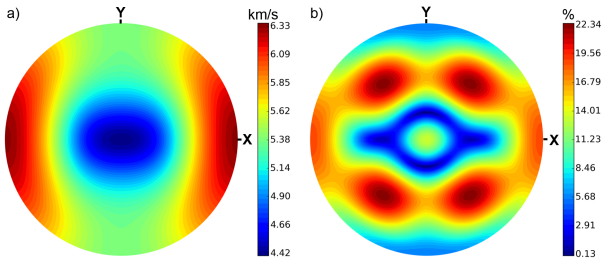

Fig. 9. V_P distribution in a hemisphere viewed along the Z direction (a) and V_S anisotropy factor distribution (b).

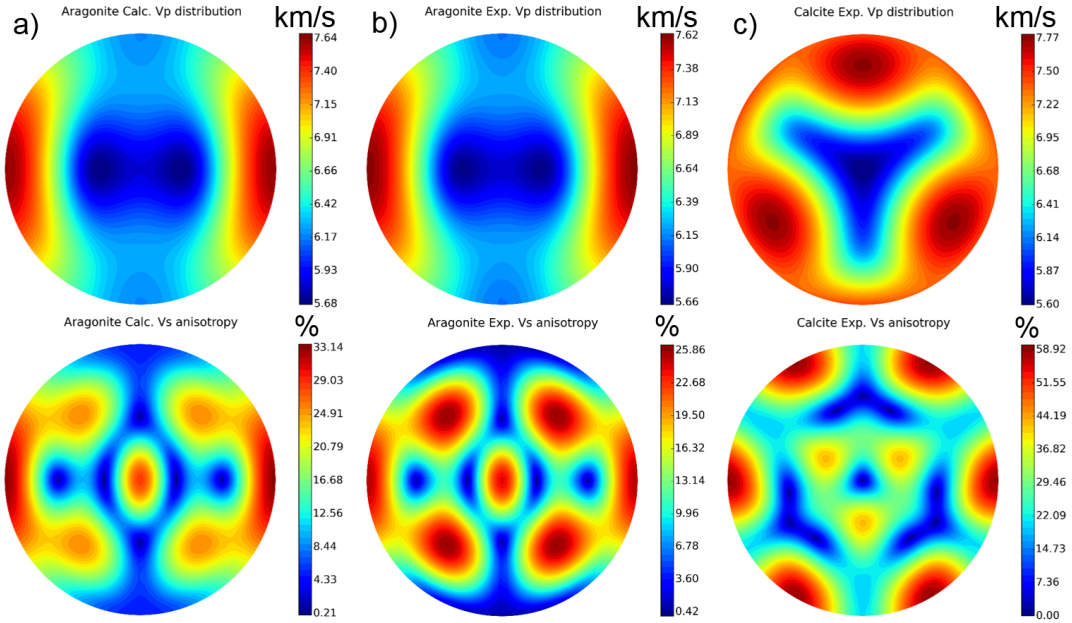

Fig. 10. Elastic anisotropy of other carbonate systems. The top row is the distribution of V_P (km/s) over a hemisphere, the bottom row is the anisotropy factor distribution of V_S (%). a): aragonite (our calculation), b): experimental values of aragonite from Liu *et al.* (2005), c): experimental values of calcite from Chen *et al.* (2001).

References

Adler, H. & Kerr, P. (1963). *Am. Miner.* **48**(1-2), 124–137. WOS:A19633762A00001.

Arapan, S. & Ahuja, R. (2010). *Phys. Rev. B*, **82**(18), 184115.

Arbeck, D., Hausshl, E., Vinograd, V. L., Winkler, B., Paulsen, N., Hausshl, S., Milman, V. & Gale, J. D. (2012). *Zeitschrift fr Kristallographie - Crystalline Materials*, **227**(8), 503–513.

Brik, M. G. (2011). *Physica B: Condensed Matter*, **406**(4), 1004–1012.

Buzgar, N. & Apopei, A. I. (2009). *Geologie Tomul L*, **2**, 97–112.

Chen, C. C., Lin, C. C., Liu, L. G., Sinogeikin, S. V. & Bass, J. D. (2001). *Am. Miner.* **86**(11-12), 1525–1529. WOS:000172417200022.

Chester, R. & Elderfield, H. (1967). *Sedimentology*, **9**(1), 5–21.

Clark, S. J., Segall, M. D., Pickard, C. J., Hasnip, P. J., Probert, M. I. J., Refson, K. & Payne, M. C. (2009). *Zeitschrift fr Kristallographie - Crystalline Materials*, **220**(5/6), 567–570.

Cromer, D. T. & Mann, J. B. (1968). *Acta Crystallographica Section A*, **24**(2), 321–324.

Dasgupta, R. & Hirschmann, M. M. (2010). *Earth and Planetary Science Letters*, **298**(12), 1–13.

Ditmars, D., Ishihara, S., Chang, S., Bernstein, G. & West, E. (1982). *J. Res. Natl. Bur. Stand.* **87**(2), 159–163. WOS:A1982NV20800002.

Dove, M. T., Hagen, M. E., Harris, M. J., Powell, B. M., Steigenberger, U. & Winkler, B. (1992). *J. Phys.: Condens. Matter*, **4**(11), 2761.

Fiquet, G., Guyot, F. & Iti, J.-P. (1994). *American Mineralogist*, **79**, 15–23.

Gillet, P., Biellmann, C., Reynard, B. & McMillan, P. (1993). *Phys Chem Minerals*, **20**(1), 1–18.

Gurevich, V. M., Gavrichev, K. S., Gorbunov, V. E., Danilova, T. V. & Golushina, L. N. (2001). *Geochem. Int.* **39**(7), 676–682. WOS:000170283400005.

Hazen, R. M., Jones, A. P. & Baross, J. A. (eds.) (2013). *Carbon in Earth*, vol. 75. Mineralogical Society of America, 1st ed.

Hill, R. (1952). *Proc. Phys. Soc. A*, **65**(5), 349.

Hossain, F. M., Dlugogorski, B. Z., Kennedy, E. M., Belova, I. V. & Murch, G. E. (2010). *Solid State Communications*, **150**(1718), 848–851.

Hossain, F. M., Dlugogorski, B. Z., Kennedy, E. M., Belova, I. V. & Murch, G. E. (2011). *Computational Materials Science*, **50**(3), 1037–1042.

Huang, C. & Kerr, P. (1960). *Am. Miner.* **45**(3-4), 311–324. WOS:A1960XF03200005.

Kraft, P., Bergamaschi, A., Broennimann, C., Dinapoli, R., Eikenberry, E. F., Henrich, B., Johnson, I., Mozzanica, A., Schleptz, C. M., Willmott, P. R. & Schmitt, B. (2009). *Journal of Synchrotron Radiation*, **16**(3), 368–375.

Krisch, M. & Sette, F. (2006). In *Light Scattering in Solid IX*, edited by M. Cardona & R. Merlin, no. 108 in Topics in Applied Physics, pp. 317–370. Springer Berlin Heidelberg.

Krishnamurti, D. (1960). *Proc. Indian Acad. Sci.* **51**(6), 285–295.

Krishnan, T. S. (1956). *Proc. Indian Acad. Sci.* **44**(2), 96–98.

Lafuente, B., Downs, R. T., Yang, H. & Stone, N. (2015). In *Highlights in Mineralogical Crystallography*. Berlin, Boston: De Gruyter.

Lashley, J. C., Hundley, M. F., Migliori, A., Sarrao, J. L., Pagliuso, P. G., Darling, T. W., Jaime, M., Cooley, J. C., Hults, W. L., Morales, L., Thoma, D. J., Smith, J. L., Boerio-Goates, J., Woodfield, B. F., Stewart, G. R., Fisher, R. A. & Phillips, N. E. (2003). *Cryogenics*, **43**(6), 369–378. WOS:000183382900006.

Ledbetter, H. M. & Kriz, R. D. (1982). *phys. stat. sol. (b)*, **114**(2), 475–480.

Lin, C.-C. & Liu, L.-g. (1997*a*). *Phys Chem Min*, **24**(2), 149–157.

Lin, C.-C. & Liu, L.-G. (1997*b*). *Journal of Physics and Chemistry of Solids*, **58**(6), 977–987.

Liu, L.-g., Chen, C.-c., Lin, C.-C. & Yang, Y.-j. (2005). *Phys Chem Minerals*, **32**(2), 97–102.

Luth, R. W. (1999). In *Mantle Petrology: Field Observations and High Pressure Experimentation: A Tribute to Francis R. (Joe) Boyd*, vol. 6, pp. 297–316. The Geochemical Society, special publication ed.

Mainprice, D. (1990). *Computers & Geosciences*, **16**(3), 385–393.

Mainprice, D., Barruol, G. & IsmaL, W. B. (2000). In *Earth's Deep Interior: Mineral Physics and Tomography From the Atomic to the Global Scale*, edited by S.-I. Karato, A. Forte, R. Liebermann, Guysters & L. Stixrude, pp. 237–264. American Geophysical Union.

Martens, R., Rosenhauer, M. & Gehlen, K. V. (1982). In *High Pressure Researches in Geoscience*, pp. 215–222. Germany.

Medeiros, S. K., Albuquerque, E. L., Maia Jr., F. F., Caetano, E. W. S. & Freire, V. N. (2006). *Chemical Physics Letters*, **430**(46), 293–296.

Medeiros, S. K., Albuquerque, E. L., Maia Jr., F. F., Caetano, E. W. S. & Freire, V. N. (2007). *Chemical Physics Letters*, **435**(13), 59–64.

Monkhorst, H. J. & Pack, J. D. (1976). *Phys. Rev. B*, **13**(12), 5188–5192.

Ono, S., Shirasaka, M., Kikegawa, T. & Ohishi, Y. (2005). *Phys Chem Minerals*, **32**(1), 8–12.

Perdew, J. P., Burke, K. & Ernzerhof, M. (1996). *Phys. Rev. Lett.* **77**(18), 3865–3868.

Plihal, M. (1973). *phys. stat. sol. (b)*, **56**(2), 495–506.

Plihal, M. & Schaack, G. (1970). *phys. stat. sol. (b)*, **42**(2), 485–496.

Rappe, A. M., Rabe, K. M., Kaxiras, E. & Joannopoulos, J. D. (1990). *Phys. Rev. B*, **41**(2), 1227–1230.

Reeder, R. J. (ed.) (1983). *Carbonates: Mineralogy and Chemistry*, vol. 11. Mineralogical Society of America.

Refson, K., Tulip, P. R. & Clark, S. J. (2006). *Phys. Rev. B*, **73**(15), 155114. WOS:000237155100038.

Sanchez-Valle, C., Ghosh, S. & Rosa, A. D. (2011). *Geophys. Res. Lett.* **38**(24), L24315.

Sanchez-Valle, C., Martinez, I., Daniel, I., Philippot, P., Bohic, S. & Simionovici, A. (2003). *American Mineralogist*, **88**, 978–985.

de Sanctis, D., Beteva, A., Caserotto, H., Dobias, F., Gabadinho, J., Giraud, T., Gobbo, A., Guijarro, M., Lentini, M., Lavault, B., Mairs, T., McSweeney, S., Petitdemange, S., Rey-Bakaikoa, V., Surr, J., Theveneau, P., Leonard, G. A. & Mueller-Dieckmann, C. (2012). *Journal of Synchrotron Radiation*, **19**(3), 455–461.

Singh, R. K., Gaur, N. K. & Chaplot, S. L. (1987). *Phys. Rev. B*, **35**(9), 4462–4471.

Skinner, A., Lafemina, J. & Jansen, H. (1994). *Am. Miner.* **79**(3-4), 205–214. WOS:A1994NG85100001.

Wang, M., Liu, Q., Nie, S., Li, B., Wu, Y., Gao, J., Wei, X. & Wu, X. (2015). *Phys Chem Minerals*, **42**(6), 517–527.

Wehinger, B., Bosak, A., Piccolboni, G., Refson, K., Chernyshov, D., Ivanov, A., Rumiantsev, A. & Krisch, M. (2014). *Journal of Physics: Condensed Matter*, **26**(11), 115401.

Winkler, B. & Milman, V. (2014). *Zeitschrift fr Kristallographie Crystalline Materials*, **229**(2), 112–122.

Winkler, B., Zemann, J. & Milman, V. (2000). *Acta Crystallogr. Sect. B-Struct. Sci.* **56**(4), 648–653. WOS:000088615200014.

Xu, R. & Chiang, T. C. (2009). *Zeitschrift fr Kristallographie - Crystalline Materials*, **220**(12), 1009–1016.

Ye, Y., Smyth, J. R. & Boni, P. (2012). *American Mineralogist*, **97**(4), 707–712.

Zhang, J. Z. & Reeder, R. J. (1999). *Am. Miner.* **84**(5-6), 861–870. WOS:000080303500021.

Synopsis

Full description of lattice dynamics and elasticity of $SrCO_3$ is reported based on a combination of first principles calculations and experimental measurements.